Relating the Radar Bright Band and Its Strength to Surface Rainfall Rate Using an Automated Approach

DONGQI LIN AND BEN PICKERING

Institute of Climate and Atmospheric Science, School of Earth and Environment, University of Leeds, Leeds, United Kingdom

RYAN R. NEELY III

National Centre for Atmospheric Science, School of Earth and Environment, University of Leeds, Leeds, United Kingdom

(Manuscript received 12 April 2019, in final form 26 September 2019)

ABSTRACT

In radar observations of hydrometeors, the 0°C isotherm in the atmosphere (i.e., the freezing level) usually appears as a region of enhanced reflectivity. This region is known as the bright band (BB). In this study, observations over 12 months from a vertically pointing 35-GHz radar and a collocated disdrometer at the Natural Environment Research Council (NERC) Facility for Atmospheric and Radio Research (NFARR) are used to identify and compare microphysical differences between BB and non-brightband (NBB) periods. From these observations, the relationship between radar reflectivity Z and rainfall intensity R is found to be $Z = 772R^{0.57}$ for BB periods and $Z = 108R^{0.99}$ for NBB periods. Additionally, the brightband strength (BBS) was calculated using a novel method derived from the Michelson contrast equation in an attempt to explain the observed variability in BB precipitation. A series of Z–R relationships are computed with respect to BBS. The coefficients increase with increasing BBS from 227 to 926, while the exponents decrease with increasing BBS from 0.85 to 0.38. The results also indicate that NBB periods identified in the presence of a 0°C isotherm in other studies may be misclassified due to their inability to identify weak brightband periods. As such, it is hypothesized that NBB periods are solely due to warm rain processes.

1. Introduction

High-quality initial observations are important for numerical models to produce accurate weather forecasts. Various instruments and methods can be used to measure precipitation, such as tipping-bucket rain gauges, disdrometers, and weather radar. The weather radar is currently the most suitable technology to measure rainfall rate R over a large area ($\sim$100 000 km^2) with high temporal and spatial resolution. Furthermore, weather radar has the ability to monitor rapidly developing events as well as tracking the speed and direction of movement of precipitation systems (Fabry 2015, chapter 1.1). However, the full potential of weather radar can be limited by errors and uncertainty in radar-based quantitative precipitation estimates (QPE). The errors and uncertainties in QPE can result from, for example, variable drop size distributions, variations in precipitation microphysics, the geometric uncertainties due to curvature of the Earth and radar beam broadening and the process of relating the measured radar reflectivity to the precipitation falling at the ground [described in, e.g., Harrison et al. (2000) and Vasiloff et al. (2007)].

In radar observations of hydrometeors, the freezing level (0°C isotherm in the atmosphere) usually appears as a region of enhanced reflectivity at a relatively constant altitude, known as the bright band (BB) (Fabry 2015, chapter 4.4.2). This occurs as ice crystals or aggregates melt and become coated in liquid, which a radar observes with the same reflectivity as a very large raindrop (Rogers and Yau 1996; Smyth and Illingworth 1998; Fabry 2015, chapter 4.4.2). Significant errors in precipitation intensity estimation can result from the enhanced radar signal of the radar BB if it is not adjusted (Joss and Waldvögel 1990). As such, various methods of BB detection and correction have been discussed in the

Denotes content that is immediately available upon publication as open access.

Corresponding author: Ryan R. Neely, r.neely@leeds.ac.uk

DOI: 10.1175/JHM-D-19-0085.1

literature and applied to national radar networks (e.g., Harrison et al. 2000; Tabary et al. 2007; Villarini and Krajewski 2010).

According to White et al. (2003) and Martner et al. (2008), the BB can be occasionally absent during stratiform precipitation. Such times are referred to as nonbrightband (NBB) periods. At Cazadero and Bodega Bay, California, Martner et al. (2008) report a statistically significant (P value of 0.01) difference in R and drop size distribution (DSD) between BB and NBB periods. Martner et al. (2008) also hypothesize that during NBB periods the precipitation can still undergo a process of freezing and subsequent melting before it reaches the surface. However, the underlying mechanism for the occurrence of NBB precipitation is not explained by Martner et al. (2008). When relating the radar reflectivity factor Z to R, the reflectivity enhancement due to the BB is corrected, but BB and NBB precipitation are not currently considered as different rain types in current operational radar-based QPE schemes, which could result in erroneous precipitation estimations.

a. *Brightband detection algorithms*

The enhanced radar return due to the BB can lead to significant errors in QPE (Harrison et al. 2000). Thus, BB detection and correction schemes are essential in order to make accurate surface rain rate estimations. The widely adopted methods for BB detection and correction analyze the vertical profiles of parameters measured by weather radar, such as radar reflectivity, Doppler vertical velocity (DVV), signal-to-noise ratio (SNR), and spectral width (e.g., Mittermaier and Illingworth 2003; Villarini and Krajewski 2010; Pfaff et al. 2014).

There are two basic approaches to detect and correct BB signals using the vertical profiles of reflectivity (VPR). One consists of applying a standardized VPR to the observed signatures. Kitchen et al. (1994) proposed a VPR correction scheme wherein the height of the brightband top (BBT) is fixed to the level of the 0°C wet-bulb temperature and the brightband width (BBW) is typically 700 m. The average error of this method is less than 150 m (Mittermaier and Illingworth 2003), but the BBT height is not diagnosed from radar itself. Rather it comes from surface synoptic observations and assumes a constant lapse rate. Another approach is to use the three-dimensional radar reflectivity to derive the brightband height (BBH), such as the scheme described in Sánchez-Diezma et al. (2000). However, VPRs are highly variable in space and time, and hence the mean or standard profiles are not sufficiently representative. A well-defined brightband bottom is often not found in the VPRs (Qi et al. 2013). The BBW also varies in different cases. Tabary et al. (2007) illustrated that 15% of the BB are thicker than typical BB while 7% of the BB are ultrathin wherein the thinnest BBW is ~20 m. In practice, the thinnest BBW that a radar is able to measure also greatly depends on the minimum gate resolution of the radar being utilized.

The BBH can also be derived by analyzing the vertical profiles of DVV with a vertically pointing radar beam. The fall velocity of hydrometeors increases in the melting layer where ice particles melt into liquid water particles and become denser with lower drag coefficients. The BB is located where a significant increase in fall velocity occurs. Pfaff et al. (2014) illustrated that a DVV algorithm is likely to derive a more accurate BBH than the algorithms analyzing VPR or the vertical gradients of VPR. Some weather radars also measure spectral width and SNR. These two parameters can be used to detect the BB, but the behavior of spectral width resembles that of the DVV (Emory et al. 2014), and the changes in SNR are similar to those seen with radar reflectivity (Pfaff et al. 2014). White et al. (2002) established an algorithm to identify BB using both the SNR and DVV. However, the thresholds for SNR can be considerably different depending on the radar. Thus, only reflectivity and Doppler velocity are considered to be suitable parameters for BB identification in this study so that the algorithms can be applied to a wide range of radars with minimal adjustment and efforts.

b. *Precipitation without a bright band (NBB)*

The absence of a BB could occur in several cases. One particular case is when solid hydrometeors do not undergo a phase change before reaching the surface. Smyth and Illingworth (1998) found that the absence of a recognizable BB was due to precipitation containing graupel. Another case is when the precipitation occurs with a warm rain process, such as a warm-frontal period described in White et al. (2003) and the supercooled warm rain process (SWRP) described in Huffman and Norman (1988), hydrometeors exist in a liquid phase from nucleation and do not freeze before reaching the surface. However, the underlying reasons why the NBB rain occurs and whether it can be also associated with melting of small ice crystals as Martner et al. (2008) hypothesized are still unclear.

White et al. (2003) examined the data of the strong El Niño 1997/98 winter from the S-Band Doppler Radar Profilers (S-PROF) at a site near Cazadero, California, and discovered that the BB was frequently not visible during nonconvective periods. White et al. (2003) concluded that NBB rain usually occurs when no part of the precipitable cloud extends above the freezing level due to a quasi-steady and shallow rain process.

White et al. (2003) found that the Z–R relationships ($Z = aR^b$) for BB and NBB periods are significantly different, and that BB rain contains more large drops and fewer small drops than NBB rain.

In combination with the S-PROF radar, Martner et al. (2008) used a Joss–Waldvögel disdrometer (JWD) to measure the DSD of the observed precipitation. Data from 11 December 2003 to 1 March 2004 at Cazadero and Bodega Bay were analyzed. Approximately half of the rainfall data were classified as occurring during NBB periods. Martner et al. (2008) illustrated the difference in DSDs and rainfall rates and found that BB/NBB DSDs are essentially the same across the mid drop size range (diameter of 0.6–2 mm) but are much different at smaller and larger drop size ranges. Accordingly, during BB periods Martner et al. (2008) found the exponent b in the Z–R relationship to be smaller, but the coefficient a to be greater. Martner et al. (2008) indicated that NBB clouds, whose echoes extend above the melting layer, do not display a melting-layer bright band because they either contain ice crystals that are too small to produce a recognizable BB [using the BB criteria of White et al. (2003)] or they are composed of supercooled liquid droplets only.

c. Brightband strength (BBS)

The aforementioned studies do not consider the impact of BBS on precipitation. Sarma et al. (2016) suggested that the microphysical properties are not only different between BB and NBB cases, but also different when BBS changes. In Sarma et al. (2016), the stratiform rain was characterized into three different types: strong bright band (strong BB) (BBW $>$ 0.49 km), weak bright band (weak BB) (BBW $\leq$ 0.49 km) and NBB. The value 0.49 km was set according to the mean BBW of the 12 stratiform events observed at National Atmospheric Research Laboratory (NARL), Gadanki, India. These observations were carried out from 1998 to 2000 using a JWD and an L-band (frequency of 1–2 GHz) wind profiler (Sarma et al. 2016). Sarma et al. (2016) found that the mean drop size is much larger for strong BB situations. Following this, Sarma et al. (2016) showed that accounting for these difference in the utilized Z–R relationships can improve QPE.

Although all these studies provided evidence that the NBB rain and BB rain are significantly different and different Z–R relationships should be adopted, their data and results are not sufficiently representative for further application. For more widespread applicability, an algorithmic study covering seasonality in precipitation is needed. White et al. (2003) only used a 21-day dataset, while only 12 stratiform cases were studied in Sarma et al. (2016). Martner et al. (2008) analyzed a 3-month dataset, but the BBs were identified manually.

Addressing this concern, Matrosov et al. (2016) extended the study of Martner et al. (2008) with a 1-yr observational period in the southeastern United States. Similarly, Matrosov et al. (2016) determined that the NBB rain should be categorized as a different rain type to yield QPE improvements. Significant underestimates (on average ~40%) in surface precipitation were found to occur if using the Z–R relationships for BB or convective rain in NBB occasions. However, the NBB rain is still not given a sole Z–R relationship in current operational radar-based QPE schemes.

2. Methods

The main purpose of this study is to propose and develop a BB/NBB detection technique that could improve radar based QPE if applied to operational observations. In addition, the Michelson contrast (Michelson 1927) is used to determine the relationship between rainfall intensity and brightband strength (BBS). Details of the instruments used in this study, algorithms and BBS calculations are described below.

a. Instrumentation

Two instruments were used in this study—a disdrometer and a radar. The disdrometer is a Thies Clima Laser Precipitation Monitor (LPM) (Adolf Thies GmbH & Co. KG 2011) deployed as part of the Disdrometer Verification Network (DiVeN) described in Pickering et al. (2019). By measuring every particle passing through its beam, the disdrometer produces a dataset of DSDs and precipitation rates. The disdrometer differentiates hydrometeors into 20 diameter bins from 0.125 to $>$8 mm, and 22 speed bins from $<$0.2 to $>$20 m s^{-1}. For a detailed specification of the instrument see Pickering et al. (2019). The Copernicus radar is a 35-GHz, vertically pointing, fully coherent, dual-polarization, pulse compression Doppler radar with antenna diameter of 2.4 m that results in a beamwidth of 0.25° (NFARR 2019). Typically, the maximum unambiguous range of Copernicus is 30 km with a maximum resolution of 30 m, and the maximum unambiguous velocity measured by Copernicus is 5.36 m s^{-1} (NFARR 2019). Echoes beyond the maximum unambiguous range or velocity are corrected (STFC et al. 2003). For a vertically pointing radar, the observational range is equivalent to the observational height.

Both instruments are located at Natural Environment Research Council (NERC) Facility for Atmospheric and Radio Research (NFARR) as shown in Fig. 1. The distance between the disdrometer and Copernicus is approximately 150 m. The time interval of the disdrometer

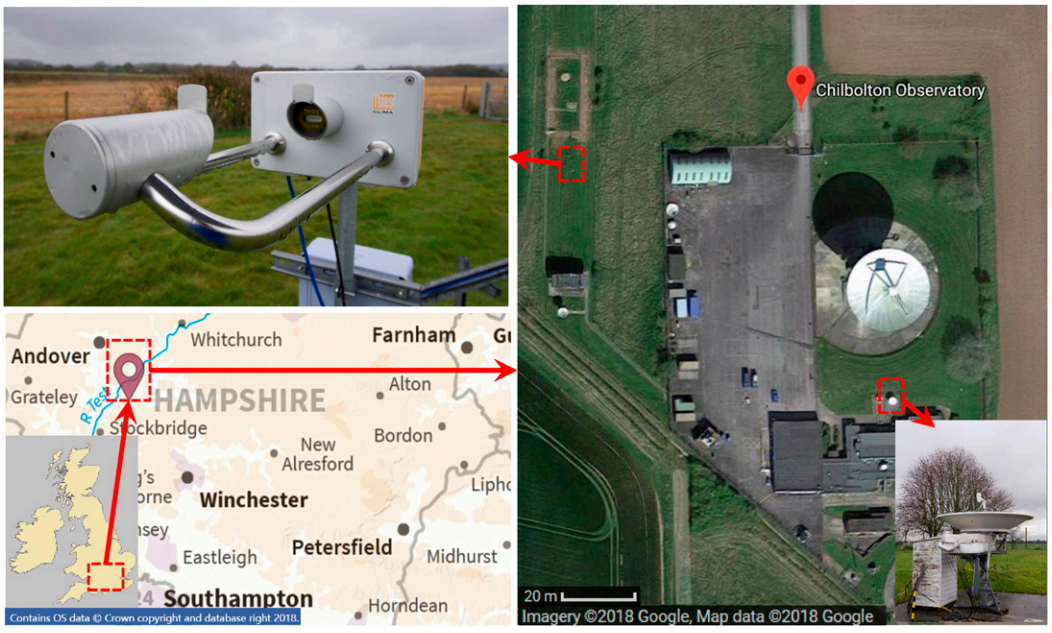

FIG. 1. Map depicting the location of NFARR and the instruments used in this study. The top-left panel shows the Thies disdrometer (image © Ben Pickering). The inset in the right panel shows the Copernicus radar. (Contains Ordnance Survey (OS) data © Crown copyright and database right 2018; imagery ©2018 Google; map data ©2018 Google).

data is 1 min. The raw disdrometer data were processed into 5-min average samples. Five minutes is long enough to provide an adequate number of samples to apply statistical methods and to mitigate uncertainties in the measurements. The typical observation cycle of Copernicus is every 45 s, while data are sometimes missing with subsequent inconsistent time intervals due to issues in data acquisition and initial processing. In this study, 5-min averages of the radar data were used to facilitate the comparison with the disdrometer data, which represent 4–6 individual vertical profiles. This also represents the periodicity of most national government-funded operational radar networks.

b. *BB identification algorithm*

Periods of BB and NBB rain referred to hereafter are periods of precipitation as classified by the following algorithms. Figure 2 is a flow diagram of the BB/NBB identification processes with the possible outcomes detailed. The details of the BB algorithm, NBB algorithm, speckle filtering, the comparison between the BB algorithm and NBB algorithm, data quality control, and calculation of BBS are presented in the following sections.

1) ALGORITHM TO IDENTIFY BRIGHTBAND PERIODS

A schematic of a vertically pointing radar observing the bright band and the standard vertical profiles of the Doppler velocity and reflectivity are shown in Fig. 3. The criteria used to partition BB and NBB precipitation is dependent on whether significant changes (i.e., a bright-band peak) exist in the Doppler velocity and radar reflectivity. Algorithms analyzing the VPR or the vertical derivative of VPR alone cannot produce ideal identification results. Hence, this study also analyzes the vertical profiles of the Doppler velocity to identify bright bands. A flowchart describing the principal steps involved in the BB identification algorithm is shown in Fig. 4a.

(i) Step 1: Detecting the BB

For vertically pointing radars, the measured Doppler velocity is the fall speed of the hydrometeors. The fall speed of a particle changes with its size and shape wherein rain and wet snow particles generally falling faster than dry snow particles when no updrafts or downdrafts are present (Yuter et al. 2006). This study classifies the dominant type of particles with fall speeds between 0.5 and 1.5 m s^{-1} as snow/ice, and the dominant type of particles with fall speeds exceeding 2.5 m s^{-1} as rain (based on Locatelli and Hobbs (1974) and Gunn and Kinzer (1949)). The BBT is the lowest altitude of snow/ice (where melting starts), while the brightband bottom (BBB) is the highest altitude of rain (where the dominant hydrometeor type is liquid). Kitchen et al. (1994) indicated that the typical BBW is 700 m but it could vary and is weighted toward narrower brightband widths (Tabry et al. 2007). Accordingly, within the algorithm, the maximum BBW is set to be 750 m

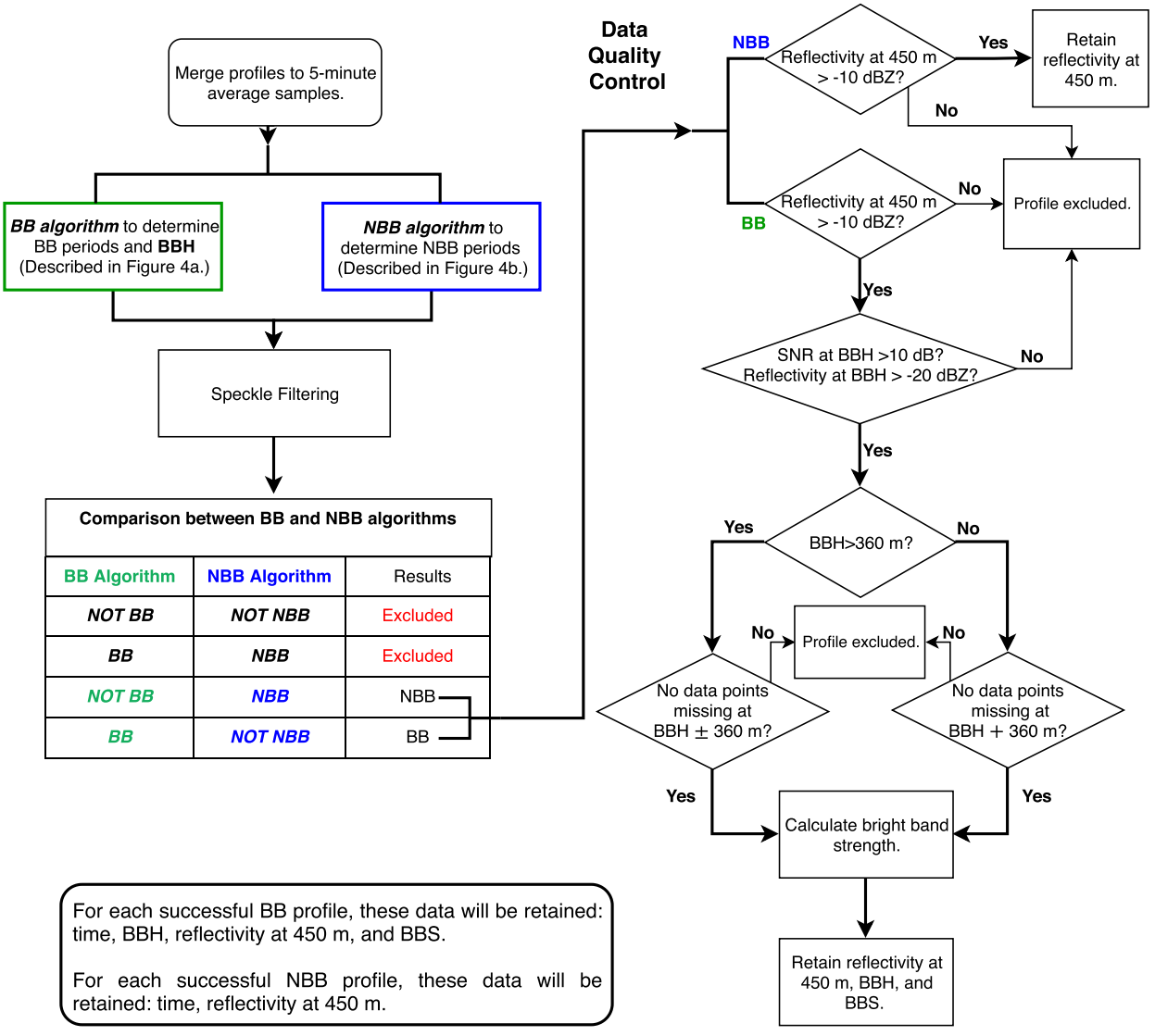

FIG. 2. Flowchart describing the outline of the BB/NBB identification processes. Text in rounded rectangles describes the outcomes.

(i.e., 25 height gates) to mitigate possible errors in BBH estimation (see Fig. 5). Otherwise, the periods with the distance between BBB and BBT over 750 m will be excluded from BB analysis.

(ii) Step 2: Locating the BBH

The Doppler velocity can be affected by vertical air motion. When updrafts or downdrafts occur, the BBB and BBT identified in step 1 can shift upward or downward by several height gates, which may lead to bias in locating the BBH. Therefore, this BB algorithm adopts the first-order vertical derivative of the Doppler velocity (∂DV) to determine the BBH. The bright band should be located where the absolute value of ∂DV is the largest because the greatest increase in the Doppler velocity is located at the height where the melting is strongest. A central difference scheme is used to compute the derivative. At a point x the first-order derivative is expressed as

$$\frac{dv(x)}{dh} \approx \frac{\Delta v}{\Delta h} = \frac{v_{(x+\Delta h)} - v_{(x-\Delta h)}}{h_{(x+\Delta h)} - h_{(x-\Delta h)}}, \tag{2.1}$$

where v is the Doppler velocity and Δh is the height interval. The minimum height interval for the central difference scheme is 60 m (the maximum height resolution is 30 m). To identify the BBH more accurately, the height interval needs to be adjusted and should not be too narrow or too wide. Figure 5 shows a schematic depicting the determination of BBH utilizing intervals

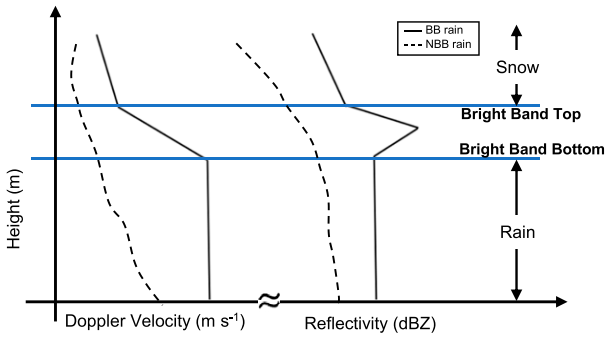

FIG. 3. Schematic showing ideal vertical profiles of Doppler velocity and reflectivity during BB (solid line) and NBB (dashed line) precipitation.

that are too narrow, too wide, and optimal. A narrow interval can lead to misidentification of the BBH due to poor-quality data near the surface and above cloud top, where a significant change in the Doppler velocity can exist within a 60-m height. When the interval is too wide, the largest change in velocity may include several hundred meters above or below the bright band. Because the algorithm has the freedom to vary the BBH by several hundred meters within a wide brightband region as shown in Fig. 5, the BBH can be misplaced when using an interval that is too wide. After several tests, the optimal interval was found to be 360 m for this study. The BBH will be used when calculating the BBS (section 2c).

2) ALGORITHM TO IDENTIFY NON-BRIGHTBAND PERIODS

Although a BB identification algorithm is established in section 2b(1), algorithms on observational data are rarely 100% accurate, particularly when considering processes with several influences such as the BB and NBB precipitation. The flow diagram of the NBB algorithm used in this study is shown in Fig. 4b. The dual-pass nature of the combined algorithm is employed in order to improve the fidelity of the overall BB/NBB classification. The first pass identifies the BB and the second identifies the presence of NBB periods. Cases where the algorithms conflict, are excluded from the study due to the lack of confidence created by the ambiguity.

(i) Step 1: Calculating derivative

During both the BB and the NBB periods, the largest ∂DV (∂DV_{max}) is always situated at the height where the Doppler velocity changes most significantly. For BB periods, this is the BBH. For NBB periods, this is where collision and coalescence occur most efficiently. As no hydrometeor type classification is performed beforehand, the height of ∂DV_{max} is marked as the location to distinguish the BB/NBB criteria.

(ii) Step 2: Detecting NBB

The criteria to identify the presence of a BB is whether there is a significant decrease in the Doppler velocity (over 1 m s^{-1}) with height within the 750-m BB region (from $\partial DV_{max} - 360$ to $\partial DV_{max} + 360$ m, i.e., the algorithm-derived BBH grid plus 360 m above and below it) (as shown in Fig. 3). Precipitation periods (i.e., when the disdrometer observed precipitation–threshold 0.1 mm h^{-1}) that do not meet these criteria are classified as possible NBB periods. Periods with poor-quality data which do not meet both the BB criteria and the NBB criteria are excluded from the study [see section 2b(4)].

3) SPECKLE FILTERING

Both the BB and NBB algorithms may misidentify some BB or NBB cases due to poor-quality data or when the specified thresholds fail to be satisfied. In addition, large random or erroneous fluctuations in the radar return signal may remain in the 5-min averages. To reduce errors and noise in the identification results, a speckle filtering scheme (Crimmins 1985; Lee et al. 1994) is applied. The speckle filtering only compares adjacent 5-min time pixels to exclude possible misidentifications of BB/NBB regardless of the BBH. The four categories of BB/NBB identification results are defined as:

- Correct BB: a BB is identified by the BB algorithm at time t with a BB detected at either time $t + 5$ min or $t - 5$ min.
- Correct NBB: an NBB is identified by the NBB algorithm at time $t$with an NBB detected at either time $t + 5$ min or $t - 5$ min.
- False BB: a BB is identified by the BB algorithm at time t but with NBB detected at both time $t + 5$ min and $t - 5$ min.
- False NBB: an NBB is identified by the NBB algorithm at time t but with BB detected at both time $t + 5$ min and $t - 5$ min.

Overall, 1390 BB profiles and 106 NBB profiles are excluded after the speckle filtering. Some BB/NBB events occurred at the beginning or the end of a precipitation period may be excluded after the speckle filtering. These events do not affect the results of this study. Only the correct BB/NBB data are used to analyze the microphysical differences because attempting to classify the false BB/NBB periods introduces further outliers in the results. Speckle filtering is also a reasonable technique to use for operational processing as it would only require a delay of 5 min for the next sample to be

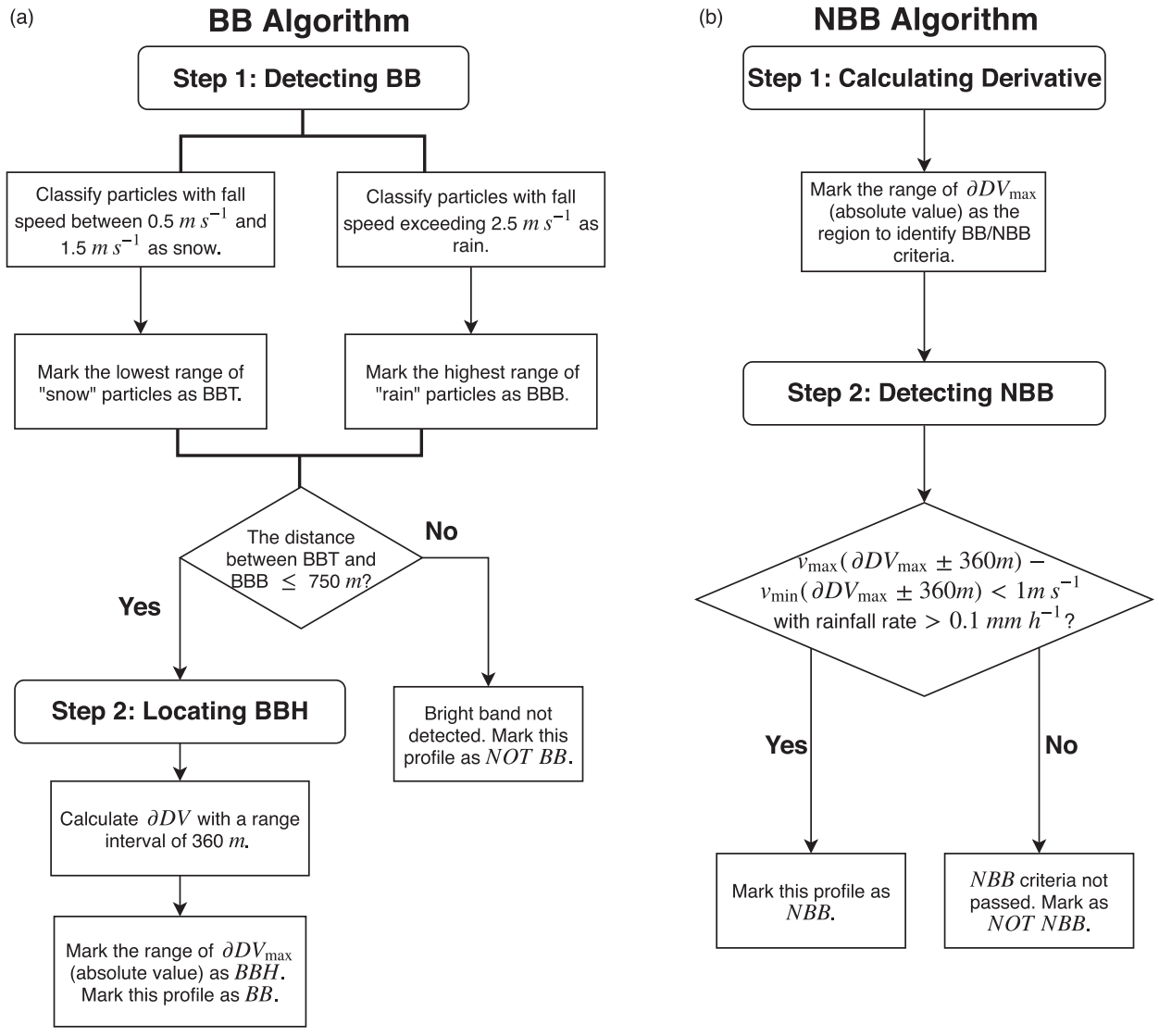

FIG. 4. Flowcharts describing (a) the BB identification algorithm and (b) the NBB identification algorithm.

made. Therefore, the method used here is directly applicable to operational schemes.

4) COMPARISON OF ALGORITHMS

As shown in Fig. 2, the combination of the BB and NBB algorithms aim to filter out periods when the BB algorithm and the NBB algorithm do not agree with each other. Namely, if the BB algorithm identifies a period as BB while the NBB algorithm classifies it as NBB, that period is considered to be a false detection and should not be used in the subsequent analysis. This circumstance only occurs three times in the total 3906 BB/NBB 5-min samples used in this study. These three samples are considered to be marginal cases, which are possibly caused by poor-quality data. Operational implementations of this algorithm may therefore choose to remove this step for computational speed and still maintain a high BB/NBB detection skill with a single-pass version of the algorithm.

5) DATA QUALITY CONTROL

A data quality control scheme (as shown in Fig. 2) is adopted because the identification algorithms can fail when the vertical profile has missing data points, such as the case shown in the dotted circle area in Fig. 5. Even though the interval of DDV calculation is adjusted, the BBH determination can still be affected by poor-quality data points.

First, the data for periods of very light rain or drizzle are more likely to be noisy. For both BB and NBB periods

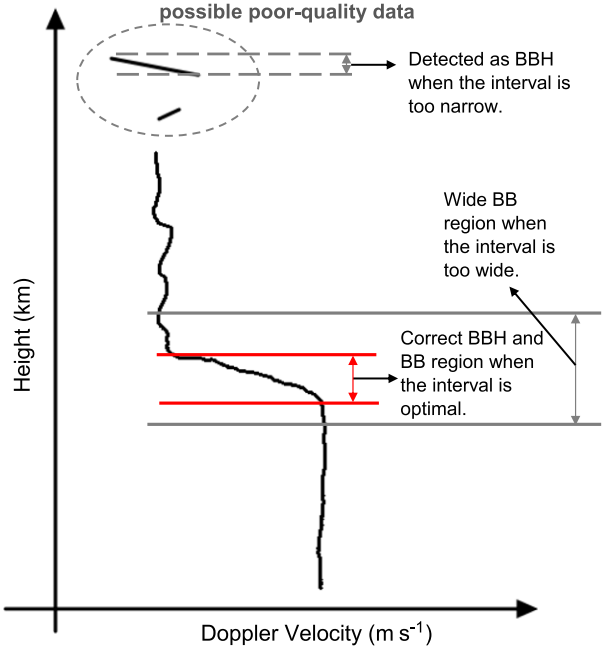

FIG. 5. Schematic of taking narrow (dotted gray), wide (solid gray), and optimal (red) intervals to compute the BBH. The dotted circle area indicates possible poor-quality data above/near the cloud top.

with the disdrometer data available, the reflectivity at 450 m should be larger than −10 dBZ and the rainfall rate measured by the disdrometer should be higher than 0.1 mm h^{-1}. Otherwise, the precipitation periods are removed.

Second, as the cloud particles have a typical radar reflectivity of −20 dBZ (Fabry 2015, chapter 3.2), if the reflectivity at the BBH identified is lower than −20 dBZ, it is not a bright band at all. The SNR at BBH must also be larger than 10 dB to ensure the radar return is of good quality.

Third, poor-quality data, which usually are shown as NaN in the Copernicus dataset, such as the dotted area shown in Fig. 5, should not exist within the brightband region, which may lead to possible false detection. If the data are of poor quality at 360 m above or below the BBH, the precipitation period is excluded from the analysis. In addition, a special case of near-ground BB is considered. The Copernicus data are only available for range gates larger than 240 m. If the height of the bright band is close to the ground (below 360 m), only data above the identified BBH are checked.

Periods that are not identified as BB and NBB periods by the algorithms and do not pass the speckle filtering and data quality control will be excluded from the analysis.

c. *Brightband strength*

Martner et al. (2008) only analyzed the $Z_{(BB,NBB)}$–R relationships using hand-picked data, whose identification is reliant upon the radar frequency as well as the contrast in the color scale used when plotting a time series of radar observations. Weak or less visible BB can easily be neglected or misinterpreted as NBB when utilizing this sort of analysis. The visibility of a BB is considered to relate to the BBS and rainfall intensity. As such, we extend the results of Martner et al. (2008) and others by examining any subsequent relation between BBS and precipitation rate. However, former studies did not introduce a reliable, repeatable, and operationally viable method to compute the BBS. Sarma et al. (2016) partitioned the strong BB and the weak BB by identifying the BBW (mentioned in section 1b), but the BBW is not solely affected by precipitation intensity. The vertical air temperature profile also controls the rate of melting. Doppler velocity and reflectivity can be enhanced significantly within a very narrow BBW [smaller than the 0.49 km set in Sarma et al. (2016)], which indicates a strong bright band. Measuring the specific amount of enhancement of the BB in every Doppler velocity and reflectivity profiles to calculate the concentrations of melting hydrometeors in the BB region is computationally expensive and infeasible in practice. Therefore, a simple and computationally efficient formula is established in this study.

As human eyes can easily distinguish the brightband location and strength, this study aimed to replicate algorithmically the way that a human would subjectively identify the "strength" of a BB in an objective manner. Humans distinguish the BBS based on the contrast of colors in the brightband region. A bright band that contrasts more with its surround reflectivity signatures by having a significant, sharp increase in reflectivity is usually subjectively identified as a stronger one. The Michelson contrast (Michelson 1927), initially used to express the visibility of interference fringes, is defined as

$$C_R = \frac{I_{\max} - I_{\min}}{I_{\max} + I_{\min}}, \tag{2.2}$$

where $I_{\max}$ is the maximum and $I_{\min}$ is the minimum intensity. This is used for the identification of periodic spatial patterns (Shapley and Enroth-Cugell 1984) as shown in Fig. 6. The Michelson contrast describes the extent of how an imaging pixel can be distinguished from its nearby pixels.

However, Eq. (2.2) cannot be used to compute the BBS directly. Higher rainfall intensity is generally associated with larger drops and more efficient collision–coalescence, even though the number of large drops is still much less than the number of small drops (Rogers and Yau 1996). In addition, radar reflectivity is more

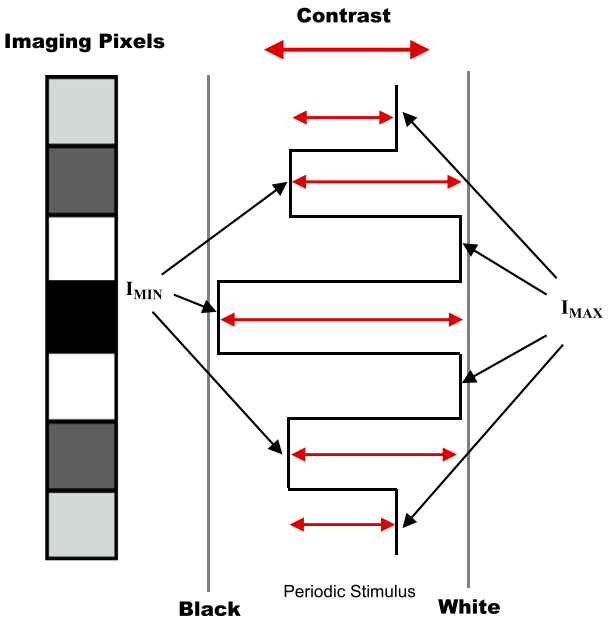

FIG. 6. Schematic showing how to measure the Michelson contrast. Transition from black to white is of higher contrast while intermediate grays are of lower contrast. (Based on Edmund Optics 2019.)

sensitive to the size of the particles than their number. Thus, hypothetically, the BBS depends on the precipitation intensity, and stronger bright bands are assumed to be associated with stronger enhancement in reflectivity, stronger melting, higher rainfall rates and larger drop sizes. When larger solid hydrometeor particles melt, a radar would observe them as much larger raindrops leading to stronger enhancement. Subsequently, within the 750-m BB region defined in this study, both the maximum and the minimum reflectivity should be higher for stronger bright bands, while the difference between the maximum and the minimum reflectivity is lower. Examples of strong BB and weak BB are shown in Fig. 7. In the strong BB case, the Michelson contrast equals to 0.24 with $Z_{max} = 34\,\mathrm{dB}Z$ and $Z_{min} = 21\,\mathrm{dB}Z$, while in the weak BB case, the Michelson contrast is 0.39 with $Z_{max} = 16\,\mathrm{dB}Z$ and $Z_{min} = 7\,\mathrm{dB}Z$. This means stronger bright bands would have smaller Michelson contrast. Hence, for the efficiency of computation, the BBS is defined as the background sum ($Z_{max} + Z_{min}$) of the BB reflectivity in the total reflectivity enhancement ($Z_{max} - Z_{min}$) of BB, which is expressed as the inverse of the Michelson contrast equation:

$$\mathrm{BBS} = \frac{Z_{max} + Z_{min}}{Z_{max} - Z_{min}}, \tag{2.3}$$

where Z_{max} and Z_{min} are the maximum and minimum reflectivity in the $\mathrm{BBH}_{\pm 360}$ region identified by the BB algorithm. Thereby, the strong BB case in Fig. 7 has a BBS of 4.23 and the weak BB case in Fig. 7 has a BBS of 2.56.

3. Results and discussion

Section 2 introduced the general vertical-structure characteristics for BB and NBB periods. In this section, a case study approach is first utilized to describe and evaluate the characteristics and algorithms used. The identification algorithms are then applied to a 12-month (11 February 2017–10 February 2018) extended observation period (EOP) to examine Z–R relationships for BB/NBB rain and assess the BBS–R relations.

a. Brightband and non-brightband precipitation

1) CASE STUDIES

Figures 8–10 show a BB case, a mixed BB/NBB case, and an NBB case, respectively. Note that weak bright bands can be spotted between 0400 and 0600 UTC in Fig. 8 and between 1030 and 1130 UTC in Fig. 9, but the rainfall rate measured by the disdrometer during those periods is below $0.1\,\mathrm{mm\,h^{-1}}$, and hence those periods are not included in the analysis and BBS computation. Figures 8–10 show that the BB/NBB algorithms are able to characterize the BB/NBB rain and identify the BBH accurately compared to human interpretation. These three cases show that the NBB rain is associated with a larger number of small drops, while the BB rain usually has fewer small drops but higher concentrations of large drops. On 1 March 2017 (Fig. 9), a BB–NBB transition is seen after 1400 UTC. The rainfall intensity remained steady, but the radar reflectivity decreased. The precipitation echo top is generally above or near the freezing level but descends rapidly during NBB periods. The profile of reflectivity is generally weaker throughout NBB periods. After the transition, large drops ($D > 0.75\,\mathrm{mm}$) almost disappear from the DSD, but the total number of small drops ($D < 0.5\,\mathrm{mm}$) increased significantly. The precipitation becomes drizzle, which is generally defined as precipitation with a drop diameter $< 0.5\,\mathrm{mm}$ (Kantor et al. 1996). The BB–NBB DSD differences in these cases agree with the inferences made by White et al. (2003) and Martner et al. (2008).

Figure 11 presents a summary of the Copernicus data for the three precipitation cases from Figs. 8–10. These contoured frequency-by-altitude diagrams (CFADs) (Yuter and Houze 1995) were produced for comparison to the CFADs described by White et al. (2003) and Martner et al. (2008). Figure 12 shows the CFADs of the 12-month EOP. The 91 296 EOP cases are split into BB and NBB events using the algorithms presented in

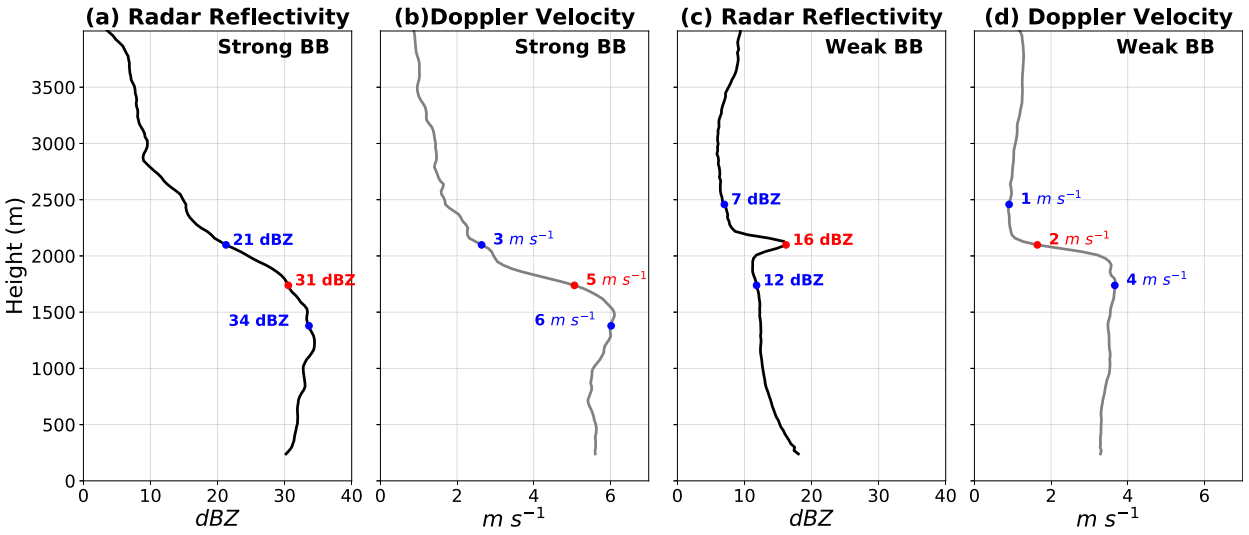

FIG. 7. Examples of vertical profiles of (a),(c) reflectivity and (b),(d) Doppler velocity during strong BB periods in (a) and (b) and weak BB periods in (c) and (d). The red dots indicate the BBH identified by the BB algorithm. The two blue dots in each subplot indicate the ranges of BBH + 360 m and BBH − 360 m, respectively. The values at these three ranges are specified in each subplot.

section 2. Figures 12c and 12f were produced using the same procedures described by White et al. (2003) and Martner et al. (2008). In these two CFADs (Figs. 12c,f), the VPR and DVV for BB precipitation were plotted as a function of distance to the algorithm derived BBH. The reference BBH at 1.85 km is the average BBH during the entire EOP and was used to adjust the VPR and DVV for BB cases. Other CFADs shown in Fig. 11 and Fig. 12 are not adjusted. In CFADs of the case studies (Fig. 11), an abrupt increase in the DVV distinguishes the BBH and BB profiles, while no prominent changes in the VPR can be recognized. The CFADs taken from the full 12-month EOP (Fig. 12) show that the BB is easily identified in an abrupt change in the DVV even though the BBH fluctuated significantly between 1000 and 3000 m throughout the period when no adjustment applied (Fig. 12b). The enhancement in the VPR can only be recognized in the adjusted CFAD (Fig. 12c). In contrast, the NBB CFADs of the case studies and 12-month observations both show that the reflectivity and the Doppler velocity increase gradually with decreasing height which is consistent with growth of liquid particles by collision–coalescence. At lower altitudes, the BB precipitation generally has larger DVV and greater reflectivity than the NBB precipitation suggesting that larger liquid particles are observed at the surface when a BB is present. The CFADs show that DVV is the key indicator of BB and NBB especially when large variability in BBH exist.

Both of the NBB precipitation events that occurred during 22 February and 1 March 2017 are suspected to have occurred due to warm rain processes. On 22 February 2017 a radiosonde launched from Herstmonceux (approximately 150 km to the east of NFARR) shows that the freezing level was well above 2000 m and therefore the radar echoes during the whole day were generally below the freezing level (Fig. 10). On 1 March 2017, the transition from BB to NBB after 1430 UTC (Fig. 9) was due to an occluded front passing over NFARR. Synoptic charts from this day show that an occluded front moved across south England bringing warmer air to NFARR, which triggered the transition in Fig. 9. Although Martner et al. (2008) reported that the echoes of NBB cases usually extend above the freezing level, this study argues that there should always be some amount of enhancement in reflectivity when ice particles melt and gain a liquid surface. When melting occurs, the size or density of hydrometeors does not appreciably change (Fabry 2015, chapter 4.4.2), but their dielectric constant increases leading to strength of the radar echo (Tiuri et al. 1984). The ability to detect a BB, however, is dependent on the radar frequency, the volume the radar observes in a single voxel, angle of observation, plotting color scale, and human interpretation. As such, within the context of the observations shown here, it is suggested that the detection techniques used by Martner et al. (2008) were unable to identify all of the BB cases that occurred. Distinguishing BB/NBB periods manually, using a radar with a less sensitive frequency and coarser spatial and temporal resolution than the Copernicus radar are likely to have led to some weak brightband periods being misclassified as NBB periods.

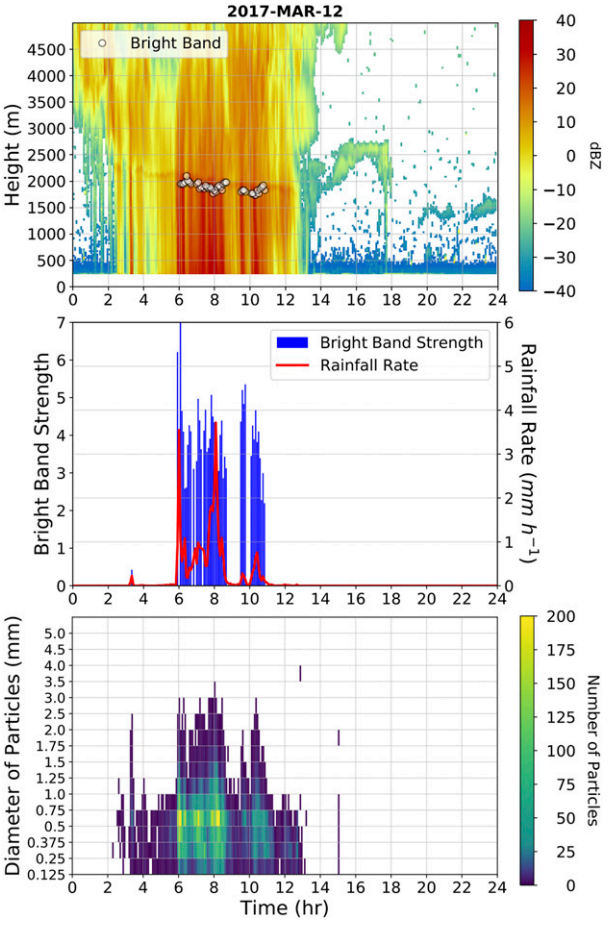

FIG. 8. A BB case. Here data are shown from Copernicus and DiVeN disdrometer data on 12 March 2017. Time is in UTC. (top) A time–height display of reflectivity. White circles indicate the BBH when a BB is detected. (middle) Time series of BBS (blue bars) and R (red line). (bottom) Contoured number of drops as a function of time and diameter (DSDs). Note that weak bright bands can be spotted between 0400 and 0600 UTC but are not marked because the rainfall rate measured by the disdrometer during this period is below 0.1 mm h^{-1}.

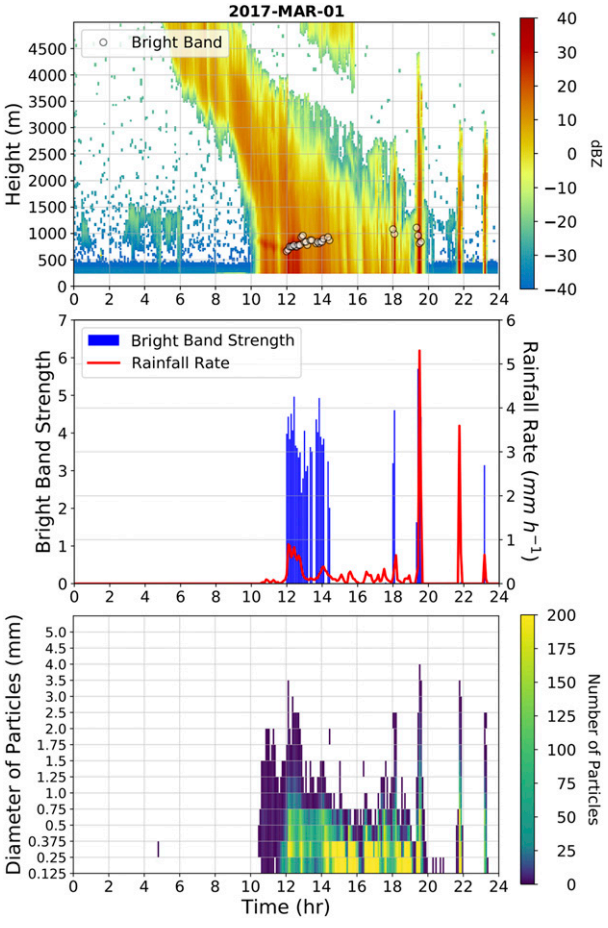

FIG. 9. A mixed BB/NBB case. As in Fig. 8, but for 1 March 2017.

NBB cases with echoes extending above the 0°C isotherm are likely to be cases of 1) supercooled liquid water droplets and/or 2) returns from cloud hydrometeors instead of precipitation. Water can exist in liquid form as cold as −38°C before the homogeneous nucleation threshold is reached (Kanji et al. 2017). In addition, Huffman and Norman (1988) concluded that ice is unlikely to form between −10° and 0°C when there are no ice crystals or large drops present. In such cases, only supercooled liquid is contained in the cold-cloud parcel. Thereby, the hydrometeors can only be formed via warm rain process, which is generally referred to as the supercooled warm rain process (SWRP) (Huffman and Norman 1988). In supercooled cases, a 0°C isotherm can be observed with liquid hydrometeors below and above while no melting occurs. Nevertheless, the dielectric constant, size, and fall speed of hydrometeors must change during melting (Tiuri et al. 1984). Subsequently, the radar, if sensitive enough, should observe a BB, while the BBS varies depending on the intensity of precipitation. However, sometimes a reduction in reflectivity below the BBB may not be observed, when the diameter of densely crystalline solid hydrometeors, such as solid ice (hail, graupel), does not significantly decrease after melting.

2) COMPARISON OF Z–R RELATIONSHIPS

As mentioned in section 2, the 5-min resampled datasets from the DiVeN disdrometer and Copernicus radar were used to compute the relationships between Z (mm^6 m^{-3}) and R (mm h^{-1}) for BB and NBB periods. Due to minor operational issues in both Copernicus and the DiVeN disdrometer during the EOP, only data from 317 days were analyzed. 91 296 profiles were processed overall, and 6280 profiles (6.9%) occurred when Copernicus was operational alongside the DiVeN

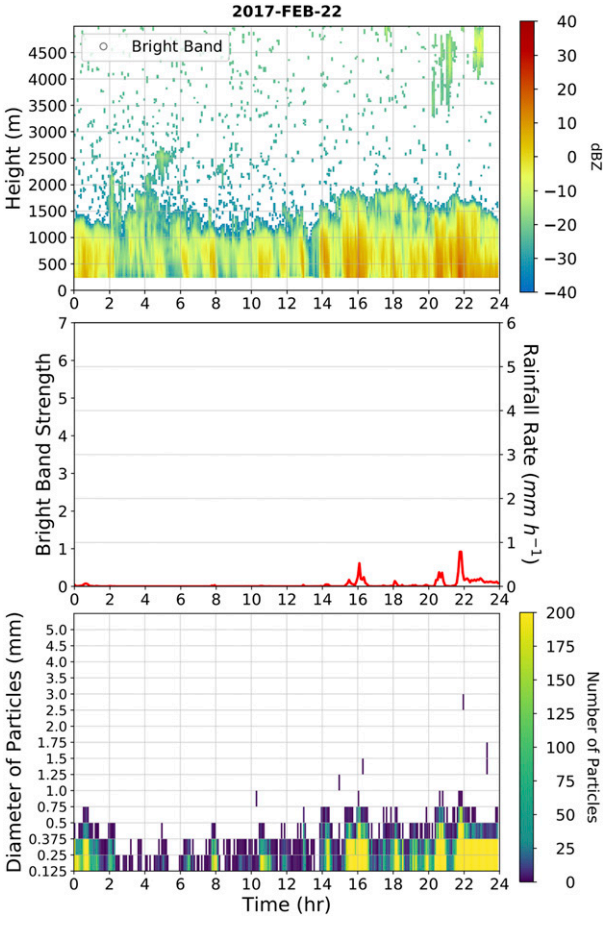

FIG. 10. An NBB case. As in Fig. 8, but for 22 February 2017.

disdrometer detecting a rainfall rate greater than 0.1 mm h^{-1}. From this subset of data, the algorithms classified 2318 (36.9%) BB samples and 1585 (25.2%) NBB samples. The remaining samples, which do not meet the BB and NBB criteria or do not pass the speckle filtering and data quality control scheme, were excluded from the analysis (37.9%). The contribution of BB and NBB precipitation to the total precipitation (583 mm) measured by the disdrometer during the EOP was 220 mm (37.7%) and 82 mm (14.0%), respectively, indicating that the BB precipitation is more intense while the NBB precipitation is not negligible. Thus, it will be important to identify NBB precipitation, if the Z–R relationships differ in BB and NBB periods.

Figure 13 shows the relative frequency distributions of the median diameter and the total number of drops from the DSDs for BB and NBB events. The BB distributions are shifted toward larger median diameters D_m and a reduced total number of drops. Approximately 85% of the NBB periods occurred with a median diameter of the DSDs less than 0.5 mm, while over 94% of the BB periods occurred with a median diameter larger than 0.5 mm. The total number of drops counted by the disdrometer was smaller than 1000 min^{-1} in 87% of the BB cases. In contrast, there is a large variation in the distribution of the drop concentration in the NBB events. These distributions agree with case studies analyzed in section 3a(1) and the results of Martner et al. (2008).

According to Martner et al. (2008), the regression calculation of Z–R relationships can be sensitive to the details of the regression technique. In this study, if the regression is calculated treating R as the dependent variable and using the R–Z relationship ($R = \sqrt[b]{Z/a}$), then the regression would give either a near-zero coefficient a or a near-zero exponent b resulting in near-constant Z–R relationships. Such regression would lead to bias in analysis. Therefore, when calculating the regressions, the Z–R relationships are in the traditional form of $Z = aR^b$ presented in Marshall and Palmer (1948). The reflectivity Z is treated as the dependent variable and a nonlinear least squares fit is used to compute the regression. Figure 14 shows the Z–R scatterplot and regressions for BB ($Z = 771.51R^{0.57}$) and NBB ($Z = 108.27R^{0.99}$) periods. Additionally, the Marshall–Palmer (M-P) relations (Marshall and Palmer 1948) applicable to precipitation measured by 35-GHz radar ($Z = 350R^{1.32}$ for rainfall rate between 0 and 5 mm h^{-1}, $Z = 450R^{1.15}$ for rainfall rate between 5 and 20 mm h^{-1}, and $Z = 780R^{0.95}$ for rainfall rate between 20 and 100 mm h^{-1}) (Table 1 in Wexler and Atlas 1963) are also shown in Fig. 14. Hereafter, these three curves for 35-GHz radar in combination are referred to as the M-P curve. The coefficient of determination (r^2) is an inadequate measure for nonlinear regressions (Spiess and Neumeyer 2010). Hence, the standard error (SE) of regression, which represents the distance between observed data and the least squares fits, is adopted to analyze the microphysical variation within the Z–R relationships. The SE for BB precipitation is 7.60 dBZ indicating that 95% of BB data points are between the regression line and ±7.60 dBZ. The SE for NBB precipitation is 4.63 dBZ. In comparison, the weighted arithmetic average SE for the M-P curve for all classes of rainfall rates is 12.90 dBZ, even though the M-P curve appears to have a good correlation with all the data points. These results suggest that separating out BB and NBB precipitation before applying Z–R relationships should lead to an improvement in QPE compared to relations that try to summarize both.

The regression is significantly affected by some outliers in the data. Although the Z–R relationships differ between BB and NBB precipitation, recognizable bias exhibit in Fig. 14 compared with Fig. 9 in Martner et al.

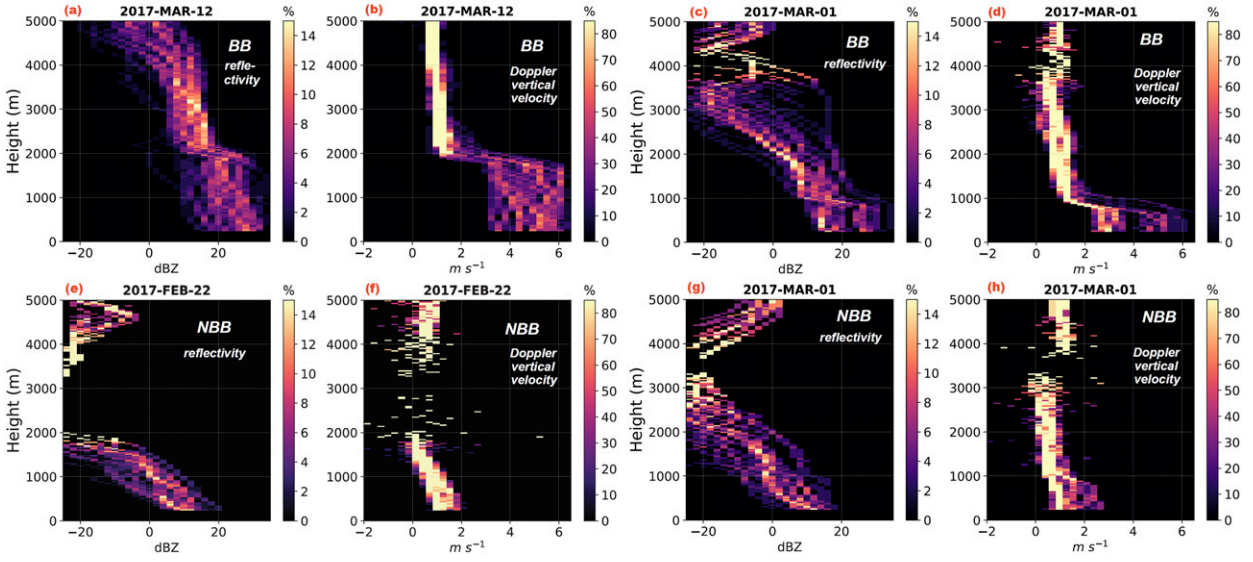

FIG. 11. Contoured frequency-by-altitude diagrams from data of the Copernicus radar at NFARR for three different days. (top) Conditions during BB events. (bottom) Conditions during NBB events. (a),(c),(e),(g) Vertical reflectivity profiles. (b),(d),(f),(h) Doppler vertical velocity (downward positive). Panels (a) and (b) are from data on 12 March 2017 with BBH at approximately 2000 m (no NBB rain detected); (c), (d), (g), and (h) are from data on 1 March 2017 with BBH at approximately 1000 m (mixed BB/NBB); (e) and (f) are from data on 22 February 2017 (no BB rain detected).

(2008). These outliers are not considered to be due to impact of updrafts and downdrafts on surface rainfall rates. Although the distance between the disdrometer and the Copernicus radar is only 150 m, differences still exist between the hydrometeors observed by the Copernicus radar at higher altitudes and those observed by the disdrometer near the surface. The falling hydrometeors may be decelerated or accelerated due

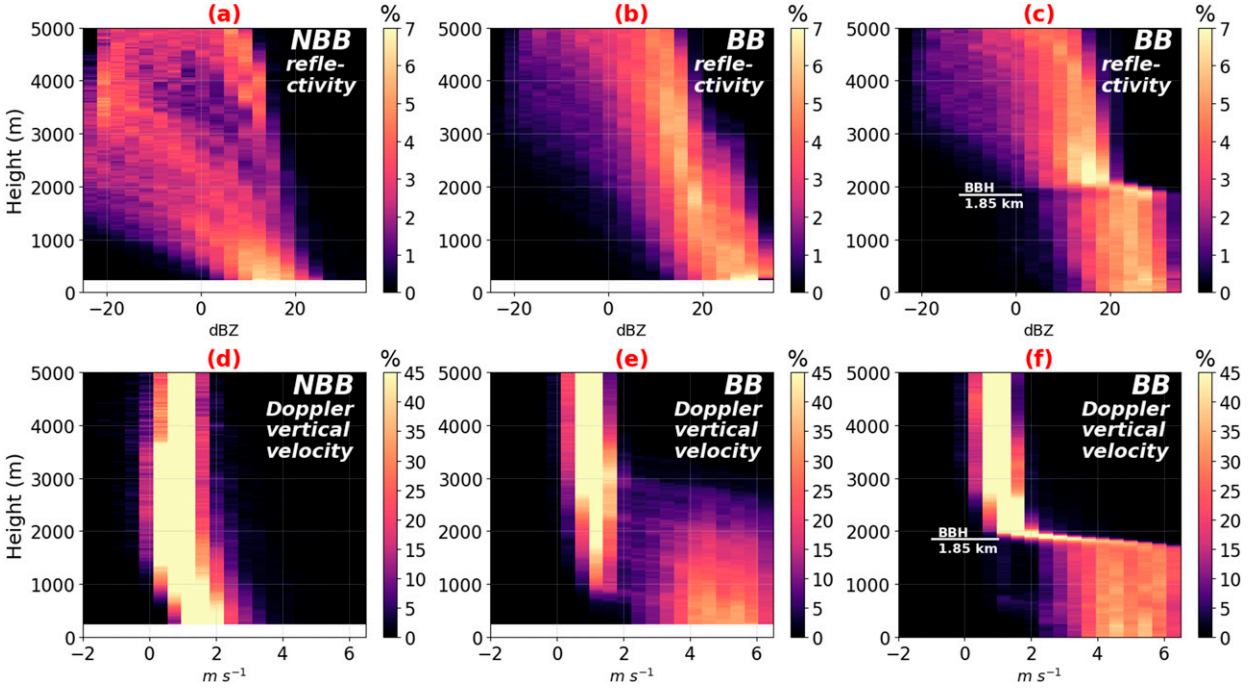

FIG. 12. CFADs from the Copernicus radar at NFARR for the 12-month EOP. (top) CFADs for vertical reflectivity profiles. (bottom) CFADs for Doppler vertical velocity (downward positive). (a),(d) Conditions during NBB events. (b),(e) Conditions during BB events. (c),(f) Conditions during BB events but the profiles are adjusted with respect to the average BBH for the entire EOP at 1.85 km, indicated by the white line.

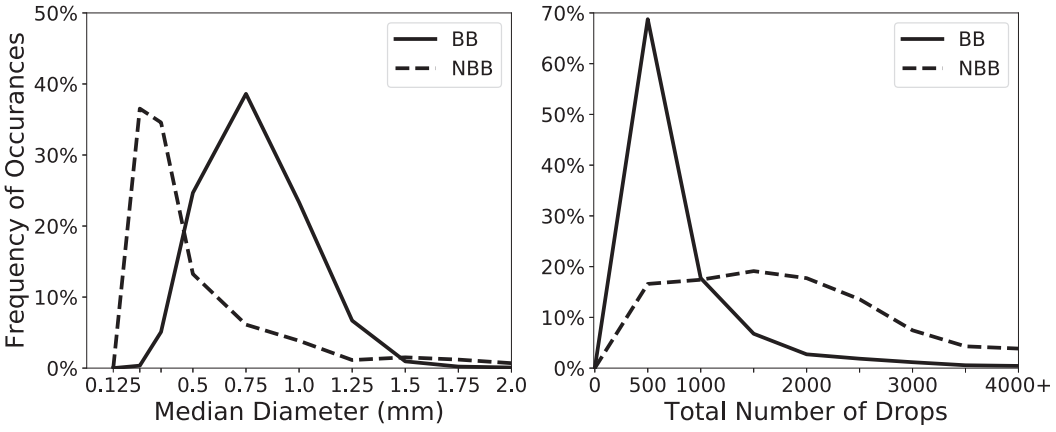

FIG. 13. Relative frequency distributions of (a) median diameter and (b) total number of drops from the DSDs measured by the DiVeN disdrometer for BB (solid curve) and NBB (dotted curve) periods.

to updrafts or downdrafts but shifting the Copernicus data by 5 or 10 min corresponding to the disdrometer data does not improve the regression. This study only considers one type of microphysical difference, BB and NBB, while the relationship between DSD, Z, and R vary with several different microphysical processes. Both the BB and NBB rain identified by the algorithm can include a mixture of different microphysical processes, such as convective rain and orographically enhanced rain (infrequent at this site but cannot be ruled out). Not all of the variability in the true Z–R relation can be explained by the BB/NBB processes alone. However, this study argues that BB/NBB modes are a dominant process and should be taken into account where possible for improved radar QPE. As seen in Fig. 14, despite some overlap between the BB/NBB Z–R points, BB precipitation is associated with generally higher reflectivity than NBB precipitation with similar rainfall rates. This is consistent with the findings of Martner et al. (2008).

b. *Brightband strength and precipitation intensity*

BBS is calculated only when a BB is detected by the algorithm in section 2b. Seven categories of BBS are used to determine subsequent Z–R relationships. These are: $0 < \text{BBS} < 1$, $1 \le \text{BBS} < 2$, $2 \le \text{BBS} < 3$, $3 \le \text{BBS} < 4$, $4 \le \text{BBS} < 5$, $5 \le \text{BBS} < 6$, and $6 \le \text{BBS} < \infty$. BBs with BBS over 3 are interpreted as strong BBs and those

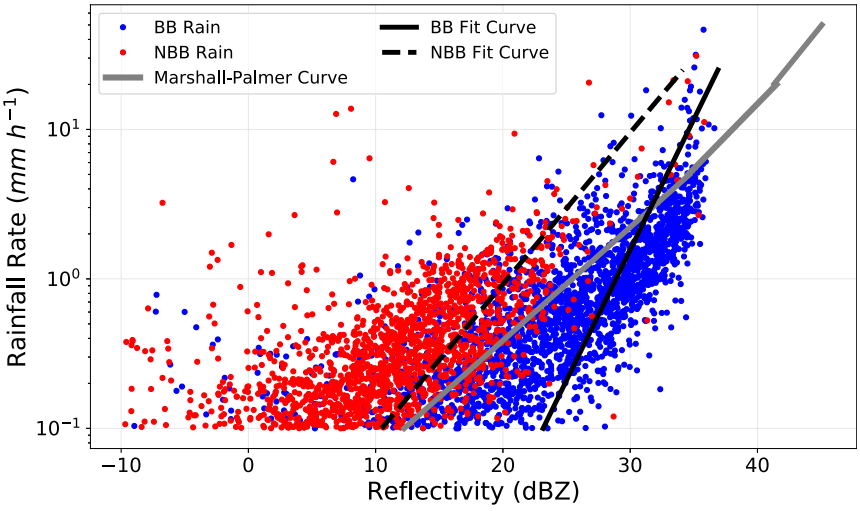

FIG. 14. Scatterplot showing Z–R relationships and best-fit regressions for BB (solid black curve) and NBB (dotted black curve). Blue circles indicate BB periods and red circles indicate NBB periods. The solid gray curves are the Z–R relationships for precipitation observed by 35-GHz radar (Marshall and Palmer 1948; Wexler and Atlas 1963). Note that the rainfall rate here is in logarithmic scale.

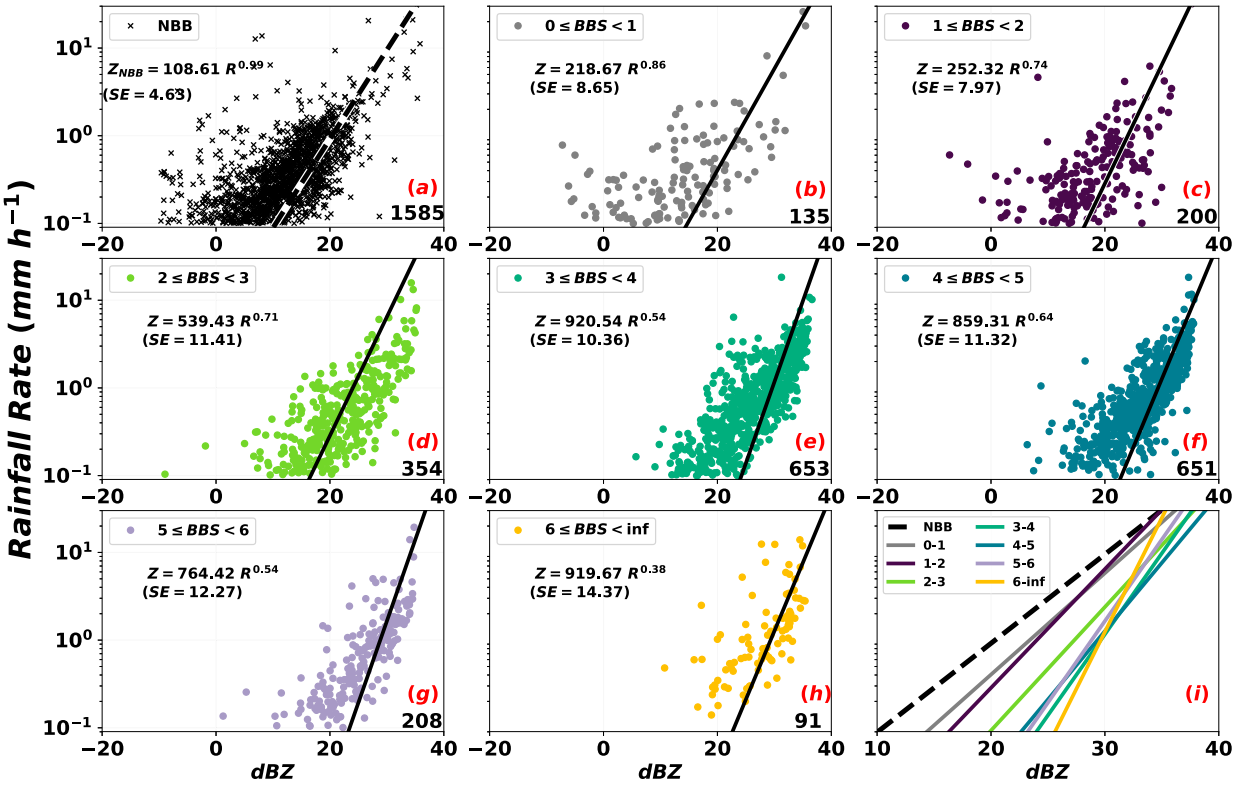

FIG. 15. Scatterplots showing Z–R relationships, best-fit regressions, and standard error (SE) of regressions for (a) NBB precipitation, (b) 0 ≤ BBS < 1, (c) 1 ≤ BBS < 2, (d) 2 ≤ BBS < 3, (e) 3 ≤ BBS < 4, (f) 4 ≤ BBS < 5, (g) 5 ≤ BBS < 6, and (h) 6 ≤ BBS < infinity. (i) The best-fit curves for all seven BBS categories. Except for (i), in each panel, the number at the bottom right indicates the number of data points in each category.

with BBS below 3 are interpreted as weak BBs. Scatterplots of the BBS and regressions are shown in Fig. 15. The corresponding Z–R relationships and determination coefficients of regressions are also presented. Figure 16 summarizes the trends of the coefficients a and the exponents b changing with respect to the BBS. Note that the SE of each Z–R relationship is an improvement over the M-P relation except for the strongest BB periods.

Figure 15 demonstrates that BB rain with higher BBS is generally associated with larger reflectivity. Apart from the category 6–∞ (due to a relatively small number of samples), the SEs of the regressions in the BBS categories are less than the SE of the M-P curve. When BBS increases, there are more data points with rainfall rate exceeding 1 mm h^{-1}. As shown in Fig. 17, BBS has a weak correlation to rainfall rate, and hence could not be used solely to prescribe rainfall rate. Nevertheless, the Z–R relationships are different with respect to BBS. The increase of BBS is associated with an increase of the coefficient a and a decrease of the exponent b. The greater the BBS is, the more the coefficients and the exponents differ from those of NBB periods. Both the increase of a and the decrease of b are nonlinear. A notable discontinuity occurs at a BBS of 3–4, where a relatively large number of samples exists. The expected reasons for the discontinuity are that 1) the issue in computing regressions due to outliers and microphysical processes other than BB and NBB [mentioned in section 3a(2)], and 2) the imperfections in the BBS calculation. Even though the pixels are not required to be adjacent for the contrast calculation described in section 2c, the data used in the visibility calculation is generally normalized (Michelson 1927), while the reflectivity data used here are not.

In addition to the Z–R relationships, Fig. 18 shows the cumulative relative frequency distributions of the median diameter from the DSDs, segregated by NBB and the seven BBS categories. All of the BB distributions are different from the NBB distribution. Generally, strong BB is associated with high concentrations of large drops ($D_m > 0.75$ mm) in DSDs, while weak BBs have high concentrations of small drops ($D_m \leq 0.5$ mm). Although strong BB generally have larger drops, the total drop concentration is much smaller (usually below 400 min^{-1} when BBS is greater than 5.5). The nonlinear correlation and scedasticity between BBS and rainfall intensity is due to the nonlinear variance of both the

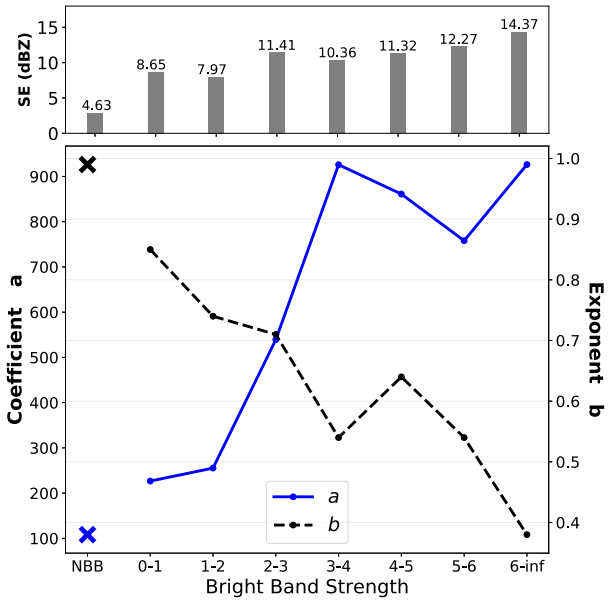

FIG. 16. (top) SE of regressions for NBB and seven BBS regressions. (bottom) Coefficients a (blue solid curve) and exponents b (black dotted curve) of the Z–R relationships for seven BBS categories. The "X" markers indicate coefficient a (108.27) and the exponent b (0.99) for NBB data.

drop size and drop concentration over rainfall rate. Therefore, strong BB cases do not always preclude a high precipitation rate. The highest rainfall rates in Fig. 17 have only a moderate BBS. Compared with the strong BB cases, the weak BB cases are more similar to the NBB cases, but that large differences between weak BB and NBB events still exist.

These results suggest that the BBS may be an indicator of the extent of ice crystal aggregation. Through this mechanism, ice crystals can aggregate into large snowflakes and become large liquid drops after melting. In general, strong BB may be associated with stronger aggregation, while the aggregation may be weaker for weak BB. In NBB cases, however, we propose that the

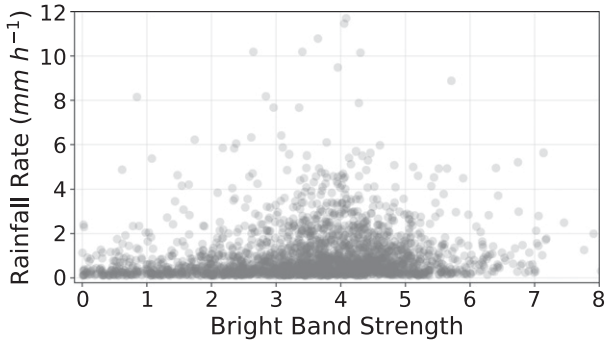

FIG. 17. Scatterplot showing rainfall rate with respect to brightband strength.

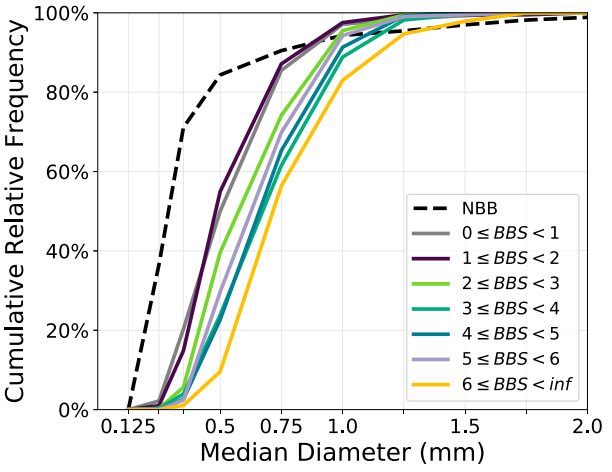

FIG. 18. Cumulative relative frequency distributions of median diameter from DSDs for NBB and seven BBS categories.

precipitation generally remains liquid growing through a process of collision and coalescence. The case of precipitation with ice crystals too small to produce a BB described by Martner et al. (2008) is hence considered as an inability to detect such a weak BB event.

Furthermore, the differences between the locations, such as topography, microphysics, and climate, can have significant impacts on the measurement of BB properties and lead to differences between this study and Martner et al. (2008). For example, orographic precipitation is the dominant precipitation type in Bodega Bay and Cazadero. However, the impact of BBS should not be ignored. Martner et al. (2008) identified that NBB rain contributed approximately 40% of the total rainfall at Bodega Bay and Cazadero, while this study found NBB rain contributed 27% of the total. The difference in BB/NBB contributions may also be an indicator of the misidentification of weak BB cases and climatic differences. Based on the observations of this study, it is hypothesized that the NBB precipitation either only contains liquid hydrometeors (due to warm rain processes) or is entirely composed of solid hydrometeors (no melting occurs).

4. Discussion and implications

The Copernicus radar has a frequency of 35 GHz, which is affected by attenuation, especially when the rainfall rate exceeds 15 mm h^{-1}. The attenuation has not been corrected in the dataset examined in this study. However, 35 GHz is in the borderline between the Rayleigh scattering regime and the Mie scattering regime for the sizes of particles being examined, and the reflectivity used to calculate Z–R relationships in section 3a(2) and section 3b is taken from near the

ground (450 m) rather than the BBH itself. In addition, in the dataset analyzed in this study, over 99% of the precipitation cases are observed with rainfall rate below 15. Hence, the attenuation effect is relatively less significant. Moreover, the purpose of this study is not to derive definitive Z–R relationships to be used directly in current operational radar networks. Instead, this work focuses on developing new methods which may be utilized to improve QPE in later studies. Thus, in this work, the attenuation is not of significant concern.

Although multiple Z–R relationships are derived in this study, these Z–R relationships are not definitive or rigorously evaluated to be utilized. The separation of BB and NBB precipitation is only an indication that the difference between BB and NBB precipitation should be considered in future operation and variability in BB precipitation can be expressed by BBS. Additionally, the SE of these Z–R relationships is relatively large. Using these Z–R relationships can lead to significant errors in rainfall rate estimation. For example, BB precipitation has a SE of 7.60 dBZ, which gives an error of 16.31 in R.

The algorithms established in this study can be applied to any vertically pointing radar, which measures Doppler velocity and deployed with a collocated instrument measuring the rainfall DSDs on the surface, to calculate the Z–R relationships for the BB and NBB precipitation. Also, most operational radars in Europe do a vertical scan for quality checks or calibration. The vertical pointing data produced by these operational radars hence can be analyzed using the BB, NBB, and BBS identification algorithms to improve radar-based QPE. Another possible instrument for the operational implications is the airborne active remote sensing radars, for example, Atmospheric Dynamics Mission (ADM-Aeolus) (described in Stoffelen et al. 2005), which measure DVV and cover vast swathes of the Earth. Future operations may consider the algorithms derived in this study in order for the improvement of QPE.

5. Conclusions

The BB is a region of enhanced reflectivity observed by a radar and is indicative of the location of the melting layer (i.e., the 0°C isotherm) within a cloud. The aim of this work was to establish a reliable and computationally effective algorithm to identify BB and NBB precipitation periods, and to verify whether BBS is related to precipitation intensity. The Z–R relationships that were calculated using Copernicus data and the DiVeN disdrometer data from February 2017 to February 2018 indicate that BB and NBB precipitation characteristics differ. Specifically, as compared to all observed BB precipitation, NBB precipitation has smaller concentrations of large drops ($D_m \geq 0.75$ mm) and larger concentrations of small drops ($D_m \leq 0.5$ mm). As such the NBB Z–R relations have a smaller coefficient a and larger exponent b. The observed DSDs studied here also confirm the microphysical inferences of Martner et al. (2008).

To further examine the role of the BB in precipitation differences, a computational method that tries to mimic the human interpretation of the BBS has been demonstrated through the use of the inverse of the Michelson contrast formula. Binning our observations into categories of similar BBS, we found that the concentration of large drops ($D_m \geq 0.75$ mm) generally increases with increasing BBS, which is also associated with a decrease in the concentration of small drops ($D_m \leq 0.5$ mm). Accordingly, in the Z–R relationships applied to BBS intervals, the coefficient a generally increases with stronger BB, while the exponent b decreases with increasing BBS. This study suggests that the hydrometeor growth during BB periods is primarily the result of ice crystal aggregation and BBS is related to the extent of aggregation, whereas the growth during NBB is dominant by collision and coalescence of water droplets.

Previous studies, such as White et al. (2003) and Martner et al. (2008), also concluded that the BB can occasionally be absent during precipitation occurring as the result of clouds that extend well above the 0°C isotherm (i.e., into regions with temperatures below 0°C). Contrary to these findings, the observations presented here provide evidence suggesting that Martner et al. (2008) may misinterpret some weak BB periods as NBB periods. Physically, the melting of solid hydrometeors should always be associated with an enhanced region of reflectivity, though the BB signature on any particular radar may not be visible depending on the BBS and radar characteristics. We suggest that precipitation periods interpreted as actual NBB processes, not weak BB periods) are due to warm rain processes.

Overall, using all available data from the EOP, we found that 36.9% of the precipitation events were classified as BB, 25.2% were classified as NBB, and 37.9% were not classified by the dual-pass algorithm. Based on the disdrometer measurements of rainfall rate, NBB precipitation contributed to approximately 14% of the total precipitation during the yearlong EOP. Hence, the NBB rainfall should not be disregarded and considering multiple Z–R relationships for different BBS and NBB events may improve radar-based QPE. However, the Z–R relationships derived in this study are not recommended to be used especially in low reflectivity situations ($Z < 5$ dBZ). We also suggest that future

studies should make use in situ observations and or hydrometeor classification algorithms to examine the differences in the physical processes between NBB and varying BB periods so that they may be better represented in weather forecast models.

Acknowledgments. The authors would like to thank the staff of the NERC Facility for Atmospheric and Radar Research (NFARR) at the Chilbolton Observatory. Without their daily vigilance and support, this work would not have been possible. We especially thank Dr. Chris J. Walden for his guidance and comments on the use of the radar data.

REFERENCES

Adolf Thies GmbH & Co. KG, 2011: Laser precipitation monitor—Instruction for use. User manual, Adolf Thies GmbH & Co. KG, 66 pp.

Crimmins, T. R., 1985: Geometric filter for speckle reduction. *Appl. Opt.*, **24**, 1438–1443, https://doi.org/10.1364/AO.24.001438.

Edmund Optics, 2019: Contrast. Accessed 20 March 2019, https://www.edmundoptics.com/resources/application-notes/imaging/contrast/.

Emory, A. E., B. Demoz, K. Vermeesch, and M. Hicks, 2014: Double bright band observations with high-resolution vertically pointing radar, lidar, and profilers. *J. Geophys. Res. Atmos.*, **119**, 8201–8211, https://doi.org/10.1002/2013JD020063.

Fabry, F., 2015: *Radar Meteorology: Principles and Practice*. Cambridge University Press, 254 pp.

Gunn, R., and G. D. Kinzer, 1949: The terminal velocity of fall for water droplets in stagnant air. *J. Meteor.*, **6**, 243–248, https://doi.org/10.1175/1520-0469(1949)006<0243:TTVOFF>2.0.CO;2.

Harrison, D. L., S. J. Driscoll, and M. Kitchen, 2000: Improving precipitation estimates from weather radar using quality control and correction techniques. *Meteor. Appl.*, **7**, 135–144, https://doi.org/10.1017/S1350482700001468.

Huffman, G. J., and G. A. Norman Jr., 1988: The supercooled warm rain process and the specification of freezing precipitation. *Mon. Wea. Rev.*, **116**, 2172–2182, https://doi.org/10.1175/1520-0493(1988)116<2172:TSWRPA>2.0.CO;2.

Joss, J., and A. Waldvögel, 1990: Precipitation measurements in hydrology. *Radar in Meteorology, Batten Memorial and 40th Radar Meteorology Conference*, D. Atlas, Ed., Amer. Meteor. Soc., 577–606.

Kanji, Z. A., L. A. Ladino, H. Wex, Y. Boose, M. Burkert-Kohn, D. J. Cziczo, and M. Krämer, 2017: Overview of ice nucleating particles. *Ice Formation and Evolution in Clouds and Precipitation: Measurement and Modeling Challenges, Meteor. Monogr.*, No. 58, Amer. Meteor. Soc., https://doi.org/10.1175/AMSMONOGRAPHS-D-16-0006.1.

Kantor, M., D. J. James, and E. W. Friday Jr., 1996: Aviation weather observations for Supplementary Aviation Weather Reporting Stations (SAWRS): Manual observations. National Weather Service Observing Handbook 8, accessed 18 February 2019, 106 pp., https://www.weather.gov/media/surface/WSOH8.pdf.

Kitchen, M., R. Brown, and A. G. Davies, 1994: Real-time correction of weather radar data for the effects of bright band, range and orographic growth in widespread precipitation. *Quart. J. Roy. Meteor. Soc.*, **120**, 1231–1254, https://doi.org/10.1002/qj.49712051906.

Lee, J. S., L. Jurkevich, P. Dewaele, P. Wambacq, and A. Oosterlinck, 1994: Speckle filtering of synthetic aperture radar images: A review. *Remote Sens. Rev.*, **8**, 313–340, https://doi.org/10.1080/02757259409532206.

Locatelli, J. D., and P. V. Hobbs, 1974: Fall speeds and masses of solid precipitation particles. *J. Geophys. Res.*, **79**, 2185–2197, https://doi.org/10.1029/JC079i015p02185.

Marshall, J. S., and W. M. Palmer, 1948: The distribution of raindrops with size. *J. Meteor.*, **5**, 165–166, https://doi.org/10.1175/1520-0469(1948)005<0165:TDORWS>2.0.CO;2.

Martner, B. E., S. E. Yuter, A. B. White, S. Y. Matrosov, D. E. Kingsmill, and F. M. Ralph, 2008: Raindrop size distributions and rain characteristics in California coastal rainfall for periods with and without a radar bright band. *J. Hydrometeor.*, **9**, 408–425, https://doi.org/10.1175/2007JHM924.1.

Matrosov, S. Y., R. Cifelli, P. J. Neiman, and A. B. White, 2016: Radar rain-rate estimators and their variability due to rainfall type: An assessment based on hydrometeorology testbed data from the Southeastern United States. *J. Appl. Meteor. Climatol.*, **55**, 1345–1358, https://doi.org/10.1175/JAMC-D-15-0284.1.

Michelson, A. A., 1927: *Studies in Optics*. University of Chicago Press, 176 pp.

Mittermaier, M. P., and A. J. Illingworth, 2003: Comparison of model-derived and radar-observed freezing-level heights: Implications for vertical reflectivity profile-correction schemes. *Quart. J. Roy. Meteor. Soc.*, **129**, 83–95, https://doi.org/10.1256/qj.02.19.

NFARR, 2019: Copernicus radar. 2 pp., accessed 3 March 2019, https://www.chilbolton.stfc.ac.uk/Pages/Copernicus.pdf.

Pfaff, T., A. Engelbrecht, and J. Seidel, 2014: Detection of the bright band with a vertically pointing k-band radar. *Meteor. Z.*, **23**, 527–534, https://doi.org/10.1127/metz/2014/0605.

Pickering, B., R. Neely III, and D. Harrison, 2019: The Disdrometer Verification Network (DiVeN): A UK network of laser precipitation instruments. *Atmos. Meas. Tech.*, **12**, 5845–5861, https://doi.org/10.5194/amt-12-5845-2019.

Qi, Y., J. Zhang, P. Zhang, and Q. Cao, 2013: VPR correction of bright band effects in radar QPEs using polarimetric radar observations. *J. Geophys. Res. Atmos.*, **118**, 3627–3633, https://doi.org/10.1002/JGRD.50364.

Rogers, R. R., and M. K. Yau, 1996: *A Short Course in Cloud Physics*. 3rd ed. Butterworth Heinemann, 290 pp.

Sánchez-Diezma, R., I. Zawadzki, and D. Sempere-Torres, 2000: Identification of the bright band through the analysis of volumetric radar data. *J. Geophys. Res.*, **105**, 2225–2236, https://doi.org/10.1029/1999JD900310.

Sarma, A. C., A. Deshamukhya, T. Narayana Rao, and S. Sharma, 2016: A study of raindrop size distribution during stratiform rain and development of its parameterization scheme in the framework of multi-parameter observations. *Meteor. Appl.*, **23**, 254–268, https://doi.org/10.1002/met.1551.

STFC, NERC, NFARR, and C. L. Wrench, 2003: Chilbolton Facility for Atmospheric and Radio Research (CFARR) Copernicus Doppler Cloud Radar Data. NCAS British Atmospheric Data Centre, accessed 1 April 2019, http://catalogue.ceda.ac.uk/uuid/e89eb9130df7817ec22cfd4b8a2ddeea.

Shapley, R., and C. Enroth-Cugell, 1984: Visual adaptation and retinal gain controls. *Prog. Retinal Res.*, **3**, 263–346, https://doi.org/10.1016/0278-4327(84)90011-7.

Smyth, T. J., and A. J. Illingworth, 1998: Radar estimates of rainfall rates at the ground in bright band and non-bright band events. *Quart. J. Roy. Meteor. Soc.*, **124**, 2417–2434, https://doi.org/10.1002/qj.49712455112.

Spiess, A. N., and N. Neumeyer, 2010: An evaluation of R 2 as an inadequate measure for nonlinear models in pharmacological and biochemical research: A Monte Carlo approach. *BMC Pharmacol.*, **10**, 6, https://doi.org/10.1186/1471-2210-10-6.

Stoffelen, A., and Coauthors, 2005: The atmospheric dynamics mission for global wind field measurement. *Bull. Amer. Meteor. Soc.*, **86**, 73–88, https://doi.org/10.1175/BAMS-86-1-73.

Tabary, P., J. Desplats, K. Do Khac, F. Eideliman, C. Gueguen, and J. C. Heinrich, 2007: The new French operational radar rainfall product. Part II: Validation. *Wea. Forecasting*, **22**, 409–427, https://doi.org/10.1175/WAF1005.1.

Tiuri, M., A. Sihvola, E. G. Nyfors, and M. Hallikaiken, 1984: The complex dielectric constant of snow at microwave frequencies. *IEEE J. Oceanic Eng.*, **9**, 377–382, https://doi.org/10.1109/JOE.1984.1145645.

Vasiloff, S. V., and Coauthors, 2007: Improving QPE and very short term QPF: An initiative for a community-wide integrated approach. *Bull. Amer. Meteor. Soc.*, **88**, 1899–1911, https://doi.org/10.1175/BAMS-88-12-1899.

Villarini, G., and W. F. Krajewski, 2010: Review of the different sources of uncertainty in single polarization radar-based estimates of rainfall. *Surv. Geophys.*, **31**, 107–129, https://doi.org/10.1007/s10712-009-9079-x.

Wexler, R., and D. Atlas, 1963: Radar reflectivity and attenuation of rain. *J. Appl. Meteor.*, **2**, 276–280, https://doi.org/10.1175/1520-0450(1963)002<0276:RRAAOR>2.0.CO;2.

White, A. B., D. J. Gottas, E. T. Strem, F. M. Ralph, and P. J. Neiman, 2002: An automated brightband height detection algorithm for use with Doppler radar spectral moments. *J. Atmos. Oceanic Technol.*, **19**, 687–697, https://doi.org/10.1175/1520-0426(2002)019<0687:AABHDA>2.0.CO;2.

——, P. J. Neiman, F. M. Ralph, D. E. Kingsmill, and P. O. G. Persson, 2003: Coastal orographic rainfall processes observed by radar during the California Land-Falling Jets Experiment. *J. Hydrometeor.*, **4**, 264–282, https://doi.org/10.1175/1525-7541(2003)4<264:CORPOB>2.0.CO;2.

Yuter, S. E., and R. A. Houze Jr., 1995: Three-dimensional kinematic and microphysical evolution of Florida cumulonimbus. Part II: Frequency distributions of vertical velocity, reflectivity, and differential reflectivity. *Mon. Wea. Rev.*, **123**, 1941–1963, https://doi.org/10.1175/1520-0493(1995)123<1941:TDKAME>2.0.CO;2.

——, D. E. Kingsmill, L. B. Nance, and M. Löffler-Mang, 2006: Observations of precipitation size and fall speed characteristics within coexisting rain and wet snow. *J. Appl. Meteor. Climatol.*, **45**, 1450–1464, https://doi.org/10.1175/JAM2406.1.